A Novel Type of Jointless HTS Induction Machine—Proof-of-Principle

Roberto Oliveira, *Senior Member, IEEE*, Tabea Arndt, Andrés Yenes, Matthias Eisele, and Marion Kläser

***Abstract*—The rotor of a commercial induction machine is replaced by a nonmagnetic, nonmetallic cryogenic rotor comprising bars of stacked 2G-high-temperature superconductors tapes without end rings nor joints, but with some back iron. The machine underwent initial functional tests with the rotor cooled by liquid nitrogen, and its operation and working principle were also verified. First, analytical considerations and finite element method (FEM) simulations are used to develop a preliminary approach to explain the machine's operation.**

***Index Terms*—Induction machine, induced magnetization, jointless rotor, partially superconducting motor, stacked high-temperature superconductors (HTS) tapes.**

Nomenclature

a	Half superconducting layer thickness [m].
f	Frequency [Hz].
i_s^s	Stator current [A].
i_s^M	Magnetizing current [A].
k	Pulses per revolution [-].
l	Active rotor length [m].
n	Power-law exponent [-].
p	Number of pole pairs [-].
s_ν	Slip for harmonic ν [-].
v_r	Rotor speed [r/min].
w	Tape width [m].
x	Rotor bar position index [-].
B	Magnetic flux density [T].
$B_\perp$	Magnetic field perpendicular to tape [T].
$B_\parallel$	Magnetic field parallel to tape [T].
B_0	Characteristic magnetic field [T].
B_a	Applied magnetic field amplitude [T].
$B_{a,\text{th}}$	Threshold magnetic field amplitude [T].
B_{c2}	Upper critical magnetic field [T].
$\hat{B}_{\delta\nu}$	Peak air-gap flux density [T].
D_r	Rotor outer diameter [m].
E	Electric field [V/m].
E_c	Critical electric field [V/m].
$I_{\nu,x}(t)$	Rotor bar current [A].
I_{c0}	Critical current at zero field [A].
$I_c(B)$	Field-dependent critical current [A].
J	Current density [A/m^2].
J_c	Critical current density [A/m^2].
J_{c0}	Critical current density at zero field [A/m^2].
L	Tape length [m].
L_{bar}	Rotor bar leakage inductance [H].
L_{ring}	End-ring leakage inductance [H].
L_g	Geometric inductance [H].
L_k	Kinetic inductance [H].
L_t	Total inductance [H].
L_M	Magnetizing inductance [H].
L_R	Rotor inductance [H].
L_σ	Stator leakage inductance [H].
L_{pole}	Pole inductance [H].
N_t	Number of HTS tapes per bar [-].
Nth	Number of counted pulses [-].
$P_{i,\text{total}}$	Electromagnetic power [W].
Q_r	Number of rotor slots; HTS bars [-].
R_{bar}	Rotor bar resistance [Ω].
R_{ring}	End-ring resistance per bar [Ω].
R_{Cu}	Copper stabilizer resistance [Ω].
R_{Ag}	Silver layer resistance [Ω].
R_h	Hastelloy resistance [Ω].
R_{sc}	Superconducting layer resistance [Ω].
R_{ac}	Dynamic AC resistance [Ω].
R_R	Effective rotor resistance [Ω].
R_s	Stator resistance [Ω].
$R_{r\nu}$	Rotor resistance [Ω].
$T_{i,\text{pole}}$	Torque per rotor pole [Nm].
$T_{i,\text{total}}$	Total electromagnetic torque [Nm].
u_s^s	Stator phase voltage [V].
$Z_{r\nu}$	Rotor impedance [Ω].
$Z_{\nu,x}$	Rotor bar impedance [Ω].
β	Field dependence exponent [-].
γ	Anisotropy factor [-].
λ	Penetration depth [m].
μ_0	Vacuum permeability [H/m].
ν	Harmonic index [-].
ρ_{FF}	Flux-flow resistivity [Ωm].
ρ_n	Normal-state resistivity [Ωm].
ρ_{sc}	Superconducting resistivity [Ωm].
$\varsigma_{r\nu}$	Rotor impedance phase angle [rad].
ϑ_x	Electrical angle at rotor bar position x [rad].

Received 3 December 2025; revised 26 March 2026 and 29 April 2026; accepted 14 June 2026. Date of publication 7 July 2026; date of current version 30 July 2026. This work was supported in part by the German Federal Ministry of Education and Research (BMBF) through the project "AppLHy!," under Grant 03HY204A and in part by the Project Management Agency Jülich (PTJ).
(Corresponding author: Roberto Oliveira.)

The authors are with the Institute of Technical Physics, Karlsruhe Institute of Technology, 76344 Karlsruhe, Germany (e-mail: roberto.oliveira@kit.edu; Tabea.Arndt@kit.edu; andres.yenes@kit.edu; matthias.eisele@kit.edu; marion.klaeser@kit.edu).

Color versions of one or more figures in this article are available at https://doi.org/10.1109/TASC.2026.3711020.

Digital Object Identifier 10.1109/TASC.2026.3711020

ω_s	Stator angular frequency [rad/s].
ω_m	Mechanical angular velocity [rad/s].
ψ_R^s	Rotor flux linkage [Wb].
Δt	Time interval between pulses [s].
$\mathbf{A}$	Magnetic vector potential [Wb/m].
$\mathbf{A}_{\text{pole}}$	Pole area vector [m^2].
$\mathbf{B}$	Magnetic flux density vector [T].
$\mathbf{B}_{s,\text{pole}}$	Magnetic flux density at pole [T].
$\mathbf{E}$	Electric field vector [V/m].
$\mathbf{J}$	Current density vector [A/m^2].
$\mathbf{T}$	Current vector potential [A/m].
$\mathbf{n}$	Surface normal vector [-].

I. Introduction

SUPERCONDUCTORS in rotating machines offer higher efficiency and higher (specific) power density—primarily when high-temperature superconductors (HTS) are used. The wide range of studies, spanning theoretical analyses, experimental prototypes, and in-field operations, focus on partially superconducting machines [1], [2], [3], [4], [5], [6], [7]. In these machines, the superconducting material is used either in the rotor or in the stator, while the other component is normal conducting.

Partially superconducting motors stand out for their practicality, often featuring HTS rotors paired with conventional copper stators. This hybrid approach mitigates cryogenic requirements by confining cooling to the rotor while leveraging superconductivity to increase torque and efficiency. Siemens' work exemplifies this, detailing 380 KW, 4 mega volt-ampere (MVA) prototypes operating at 3600 r/min with HTS rotor windings [1], [2], [3]. These machines achieved efficiencies 2% higher than conventional generators, with successful inverter-driven operation, highlighting their viability for ship propulsion and variable-speed drives. In wind power applications, 1 MW synchronous generator was developed using 2G-HTS field windings [4], reducing the machine size by 1.75 times and its mass to 1.5 t. Cryogenic cooling of the rotor via liquid nitrogen (LN_2) allowed for low losses (below 1.6%), making it ideal for offshore turbines. This approach has been extended to multi-MW direct-drive generators [8]. More recently, the Speedy_HTS project demonstrated the replacement of a conventional permanent magnet rotor with a 2G-HTS rotor in a mid-speed wind power generator, effectively doubling the power density [7].

For induction/synchronous hybrid machines (HTS-ISMs), theoretical analyses of yttrium barium copper oxide (YBCO) squirrel-cage rotors have demonstrated substantial enhancements in starting and accelerating torque, attributed to persistent current effects and magnetic flux trapping [9], [10], [11]. Experimental investigations have further confirmed the hysteretic rotational behavior of HTS-ISMs [5], [12]. More recent electromechanical studies of HTS cage rotors have identified the coexistence of slip and synchronous operating modes, arising from the resistive–superconducting duality inherent to HTS tapes [6]. Recent advances in axial-flux topologies employing HTS tapes in the rotor have demonstrated improved flux density and reduced stator complexity, with detailed core-loss analyses [13]. Compact liquid hydrogen-cooled HTS motors have also been proposed, featuring disk-up-down assembling coil configurations suitable for fully and partially superconducting architectures, optimized for fuel cell-based electric propulsion systems [14], [15].

Comparative studies indicate that partially superconducting motors often outperform fully superconducting counterparts in terms of reliability, cost, and efficiency, as cryogenic requirements are localized [16]. Reviews of HTS rotating machines classify designs by superconductor form—wires, bulks, or stacks—and highlight the suitability of partially superconducting configurations for high-torque, low-speed applications, such as wind turbines and marine propulsion [17], [18]. Fully superconducting machines continue to lead in specific power, as exemplified by aerospace. In summary, while fully superconducting machines push the limits of power density, partially superconducting systems represent a practical and near-term pathway, combining the advantages of HTS technology with the robustness of conventional designs.

Today, there is a considerable market share of very robust and simple conventional induction machines, and replacing these machines with HTS-based machines may be attractive for a broad range of applications (e.g., in industry and locomotives) [19], [20], [21], [22]. The apparent benefit of asynchronous machines is the simplicity of the rotor, which eliminates the need for current feeding and control. For superconducting induction machines, some modeling and experimental verification have been reported [9]. However, all approaches so far have followed the concepts of machines based on conventional topologies, i.e., radial flux machines, axial flux machines, synchronous machines with either constant magnetization or field windings, and asynchronous machines that replace the normal conducting rotor with a cage of soldered HTS wires [10], [11], [12], [13].

This work addresses the question of whether it is possible to simplify a squirrel-cage machine using appropriate HTS significantly. The basic idea is to omit the end rings of the squirrel cage and replace the bars with stacks of HTS rare-earth barium copper oxide (REBCO) tapes (2G-HTS), eliminating the need for soldered electrical connections. To some extent, this approach resembles the operation of an HTS dynamo [23].

This yields a novel type of rotating machine—for simplicity, it is referred to as a "stacked tape architecture rotor (STAR)-machine."

II. Methodology

To address the research question, the following steps were carried out: experimental realization of a first-of-its-kind machine, basic electromagnetic description of the machine, FEM analysis, and analytical considerations.

A. Experimental Realization of a First STAR-Machine

The STAR-motor incorporates a rotor constructed by the stacking of 2G-HTS tapes to form the rotor bars. As illustrated in Fig. 1, these HTS bars are not connected by short-circuiting end rings but simply stacked metal-on-metal. This realization does not require any soldering processes. Previous work [7], [24] has shown that a typical metal-to-metal interface, as processed in our labs, yields specific contact resistivities on the order of 85

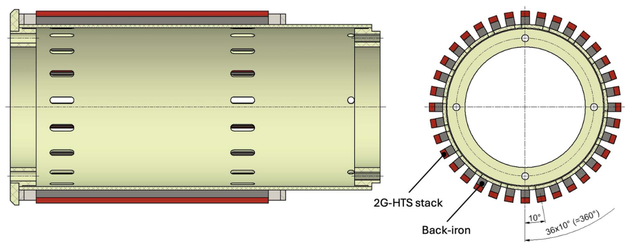

Fig. 1. Rotor body (FRP, yellow) with stacked HTS tapes (red) and laminated back iron (gray).

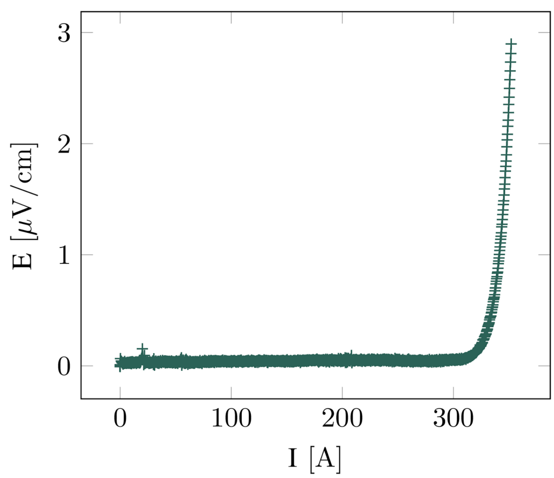

Fig. 2. Measured electric field E versus current I characteristic of the 2G-HTS used for the rotor bars (2014 delivery of 5 mm-wide Fujikura FESC series).

TABLE I
MAIN PARAMETERS OF THE EXPERIMENTAL MACHINE

Stator	Value	HTS Rotor	Value
Outer radius [m]	0.0915	Outer radius [m]	0.0555
Inner radius [m]	0.0590	Inner radius [m]	0.0480
N. of Poles [-]	4	Number of bars [-]	36
Slot/pole/phase [-]	3	Length [m]	0.135
Op. Temperature [K]	≈300	Op. Temperature [K]	≈77
Current [A]	7.1	Physical Air gap [m]	0.00325
Voltage [V]	35.35	[1]Mag. Flux Density [T]	0.2
Frequency [Hz]	0–50	Rotational Speed [r/min]	0–1500

[1]Magnetic flux density in the air gap (rotor outer radius)

mΩcm^2. Since the impregnation process is expected to preserve this value, the resulting tape-to-tape resistance is 85 mΩcm^2 / (0.5 · 13.5) cm^2 = 13 mΩ. However, because the induced currents predominantly flow in-plane of the HTS tapes rather than across the tape-to-tape interfaces, this contact resistance has no effect on torque production.

To improve the magnetic field profile across the bars, each bar is backed by a laminated electrical steel assembly, specifically of the M530 grade. The entire bar (2G-HTS and M530) is epoxy-impregnated. The bars are aligned parallel to the rotor's axis. The rotor body is made out of fiber-reinforced plastics (FRP) and thus magnetically transparent. The principal design parameters are detailed in Table I. In Fig. 2, the electric field versus current characteristic of the used 2G-HTS tapes is presented.

For the sake of simplicity and speed in the realization of the machine, the (commercially available) stator consists of three-phase copper windings and a laminated magnetic core (see Table I). However, this will limit the machine's operational regime. The original induction motor has a total mass of 44 Kg (stator of 29.6 Kg, fan and cover are 1.8 Kg, and the rotor is 12.6 Kg). The STAR-machine configuration, when accounting for the LN_2-filled assembly, achieves a mass of 36.53 Kg (29.6 Kg+6.93 Kg).

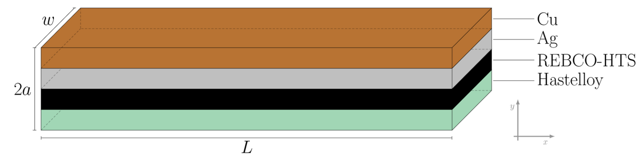

Fig. 3. Schematic sketch of the 2G-HTS tape, its layers, and the main dimensions.

B. Basic Electromagnetic Description of the STAR-Machine

In a conventional squirrel-cage induction motor, the current traversing any rotor bar is calculated by dividing the induced electromotive force (emf) by the rotor impedance, as described by (1). The parameters are delineated as follows [25]: index ν indicates the νth harmonic, $\hat{B}_{\delta\nu}$ represents the peak magnitude of the air gap flux density, $\vartheta_x = xp\vartheta$ denotes the electrical angle at the mechanical position of the bar x, s_ν represents the slip associated with the induced emf, $\varsigma_{r\nu}$ corresponds to the phase angle of the rotor impedance, D_r indicates the rotor's outer diameter, and l is active rotor length. The impedance of the rotor is characterized by (2), where ω_s is the stator angular frequency, R_{RING} is the resistance of the end-ring segment per bar, L_{BAR} and L_{RING} are the leakage inductances of the bar and its associated end-ring section, respectively, and Q_r represents the number of rotor slots

$$\hat{I}_{\nu,x}(t) = \frac{s_\nu \omega_s}{2p\nu} \frac{\pi D_r l}{Z_{r\nu}} \hat{B}_{\delta\nu} e^{j[s_\nu \omega_s t - \nu\vartheta_x - \varsigma_{r\nu}(s_\nu)]} \tag{1}$$

$$\begin{aligned}\underline{Z}_{\nu,x} &= R_{r\nu} + j\omega_s L_{r\nu}\\ &= \left(R_{\text{BAR}} + \frac{R_{\text{RING}}}{2\sin^2(\frac{\nu\pi p}{Q_r})}\right) + j\omega_s \left(L_{\text{BAR}} + \frac{L_{\text{RING}}}{2\sin^2(\frac{\nu\pi p}{Q_r})}\right).\end{aligned} \tag{2}$$

In the present work, the STAR-rotor omits short-circuit rings, as shown in Fig. 1. Consequently, the complexity of the rotor impedance model (2) is significantly reduced, as it obviates all terms associated with the ring. It is imperative to evaluate the per-bar HTS resistance and inductance during the analytical phase of the design procedure. Each HTS bar is constructed from tapes that incorporate a Hastelloy substrate, an active superconducting layer, a silver layer, and a copper stabilizer—see Fig. 3. Thus, the total resistance of the bar can be expressed using (3), where N_t is the number of HTS tapes

$$R_{\text{BAR}} = \left(\frac{1}{R_{\text{Cu}}} + \frac{1}{R_{\text{Ag}}} + \frac{1}{R_{\text{sc}}} + \frac{1}{R_h}\right)^{-1} \cdot \frac{1}{N_t} \approx \frac{R_{\text{sc}}}{N_t}. \tag{3}$$

The current path within the HTS tapes forms a closed loop that encompasses the surface area of each individual tape, as

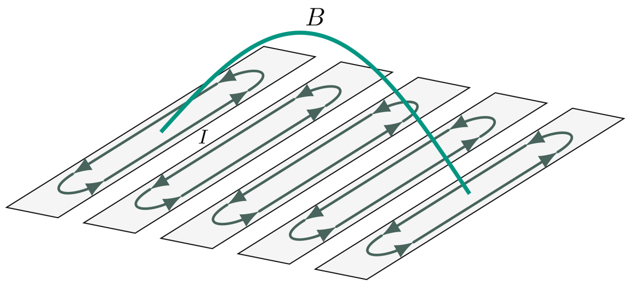

Fig. 4. Rotor current paths are closed within the individual HTS tapes.

illustrated in Fig. 4. Under the magnetoquasistatic (MQS) approximation, the Ampère–Maxwell law can be written as

$$\oint_C \mathbf{H} \cdot d\mathbf{l} \approx \iint_S \mathbf{J} \cdot d\mathbf{A} \tag{4}$$

with C an Ampère loop that surrounds the tape completely. In addition, assuming negligible charge accumulation within the conductor the continuity equation under MQS conditions is given by

$$\nabla \cdot \mathbf{J} = 0 \tag{5}$$

which implies that current lines cannot originate or terminate inside the material.

The tape is galvanically isolated because of the stacked-tape architecture. Consequently, the net current crossing any surface S that cuts the tape transversely must vanish, meaning that no net transport current flows through the tape. Equations (5) and (6) together imply that the currents must circulate within the tape

$$\iint_S \mathbf{J} \cdot d\mathbf{A} = 0. \tag{6}$$

The induced current in the rotor exhibits a component predominantly in the axial direction of the machine, i.e., longitudinally along the tapes as depicted. In the presence of a radial magnetic field, this axial current component gives rise to a tangential Lorentz force, which is responsible for torque production in the machine. At the same time, the circulation of current within the rotor necessarily implies the presence of additional transverse components of current density within the tapes, which may lead to force components in other directions depending on the local magnetic-field distribution.

The relatively large resistances of the silver and copper components are primarily attributed to their small cross sections.

The current density within the superconducting layer follows a power–law relationship in (7), with its dependence on the magnetic field described in (8) [26]. The nonlinear resistivity in the superconductor, under conditions of trapped flux (ρ_{sc}) and flux flow (ρ_{FF}), is described by (9) and (10), respectively, where ρ_n represents the resistivity in the normal state [27], [28], [29]

$$J = J_c \left(\frac{E}{E_c}\right)^{1/n} \tag{7}$$

$$J_c(B_\perp, B_\parallel) = \frac{J_{c0}}{\left(1 + \frac{\sqrt{B_\perp^2 + B_\parallel^2/\gamma^2}}{B_0}\right)^\beta} \tag{8}$$

$$\rho_{\text{sc}} = \frac{E_c}{J_c}\left|\frac{J}{J_c}\right|^{n-1} \tag{9}$$

$$\rho_{\text{FF}} \approx \rho_n \frac{B}{B_{c2}}. \tag{10}$$

The electrical resistance exhibited by a type-II superconductor is described by (11), where S_{sc} denotes the effective cross section of current flow and L is the length of the sample. The dynamic resistance resulting from the losses of the alternating current (AC)—as defined in (12) [30], [31]—integrates the active thickness $2a$ of the superconducting tape (depicted in Fig. 3), the maximum amplitude of the applied magnetic field B_a, and the threshold field amplitude $B_{a,\text{th}}$. This AC loss model is interconnected with the magnetic field dependence of the critical current, as described in (13), with the characteristic field B_0. The field-dependent critical current $I_c(B)$ influences the flux penetration, and therefore the magnitude of the dynamic resistance as expressed in (12) [32], [33]

$$R_{\text{sc}} = \int_L \frac{E_c J^{n-1}}{\left[J_{c0} \Big/ \left(1 + \frac{\sqrt{B_\perp^2 + B_\parallel^2/\gamma^2}}{B_0}\right)^\beta\right]} S_{\text{sc}} dL \tag{11}$$

$$R_{\text{ac}} = \frac{4afL}{I_{c0}}\left(B_a - B_{a,\text{th}}\right) \tag{12}$$

$$I_c(B) = \frac{I_{c0}}{1 + B_a/B_0}. \tag{13}$$

In an elongated and narrow superconducting tape characterized by its length L and width w, the geometric inductance is influenced by the external magnetic field. It can be approximately expressed, assuming that the geometric relations $L \gg w \gg a$ hold, by (14)

$$L_g \approx \frac{\mu_0 L}{2\pi}\left[\ln\left(\frac{2L}{w + 2a}\right) + 0.5\right]. \tag{14}$$

This formulation is derived from classical current-sheet models and has been substantiated through various studies [34], [35]. In addition to this, the kinetic inductance, as given by (15), originates from the inertia of Cooper pairs confined within the superconducting penetration depth λ [36]

$$L_k = \mu_0 \lambda^2 \frac{L}{2a \cdot w}. \tag{15}$$

For a thin tape that supports current on both surfaces, this has been rigorously established in the context of 2-D flux-pinning models. Consequently, the total inductance is simply the arithmetic sum: $L_t = L_g + L_k = 1.2120{\cdot}10^{-7}$H.

The per-phase equivalent circuit representation of the STAR-machine is illustrated in Fig. 5—based on the work presented in [9], [37], [38], and [39]. An electrical potential difference, denoted $\underline{u}_s^s$, is introduced at the stator terminal, which energizes a series configuration that includes the resistance of the stator

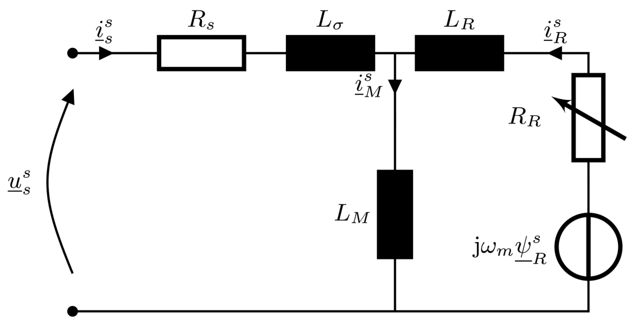

Fig. 5. Simplified per-phase equivalent circuit of the STAR-machine (slip-mode: $R_R > 0$ and synchronous mode: $R_R = 0$).

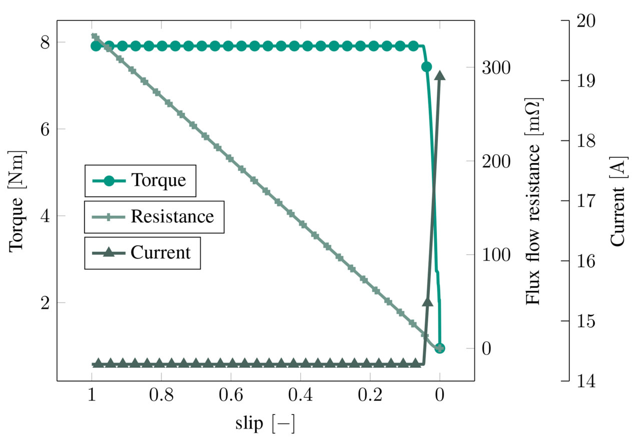

Fig. 6. Torque, flux-flow resistance R_R, and rotor current of the STAR-machine versus slip according to the equivalent circuit.

winding R_s and the leakage inductance of the stator L_σ. This series arrangement is subsequently connected to a parallel magnetizing branch characterized by the mutual inductance L_M.

The rotor circuit includes the effective HTS resistance R_R and the rotor inductance L_R. At slip $s = 1$ (i.e., at startup), the induced rotor current reaches its maximum, and the associated losses are dominated by flux-flow resistance. As the rotor accelerates, the induced rotor current, which is proportional to slip ($\propto s$), progressively decreases. During this process, the superconductor may start trapping the magnetic flux.

Consequently, the effective resistance of the superconductor varies with current density, field variation rate, and field amplitude (11). This variation of the magnetic field can generate losses characterized by dynamic resistances (12). The inductance of the rotor only modifies the phase relationship between the applied flux and the induced current.

The voltage source $j\omega_m \underline{\psi}_R^s$ models the magnetized HTS strips, which exhibit quasi-permanent-magnet behavior. Here, ω_m denotes the mechanical angular velocity, and $\underline{\psi}_R^s$ represents the rotor magnetic flux linkage referred to the stator.

Fig. 6 illustrates the torque and rotor current, alongside the rotor effective resistance, as calculated from the equivalent circuit analysis for 50 V at 50 Hz, maximum torque of 7.91 Nm@s =1 to 0.01, synchronous torque of 0.94 Nm and $R_{2,(s=0.01,0.001)} = 5.81{\cdot}10^{-4}\Omega$ to $1.012{\cdot}10^{-4}\Omega$.

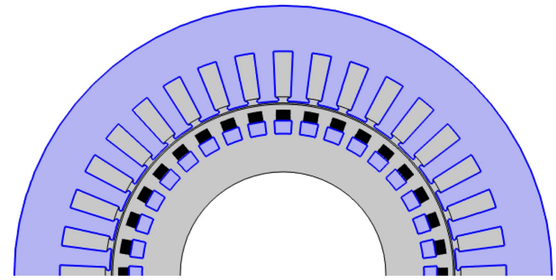

Fig. 7. FEM model geometry (electrical steel in blue).

C. Simulation

A computational framework has been formulated to investigate the operational characteristics of a partially HTS motor (see Fig. 7). This methodology utilizes established electromagnetic modeling techniques specific to superconductivity, particularly the T–A formulation [40], [41]. The relationship between the magnetic vector potential $\mathbf{A}$ and the current density $\mathbf{J}$ is derived from the equation

$$\nabla \times \left(\frac{\nabla \times \mathbf{A}}{\mu_0} \right) = \mathbf{J} \tag{16}$$

where μ_0 represents the vacuum magnetic permeability and $\mathbf{J}$ is the sheet-like current distribution on the surface of the HTS tape. This relation is a direct consequence of applying vector identity to the curl of the magnetic field.

Ampère's law, in its differential form, establishes the connection between the curl of the magnetic induction $\mathbf{B}$ and the current density $\mathbf{J}$, where $\mathbf{B}$ is defined as the curl of the vector potential: $\mathbf{B} = \nabla \times \mathbf{A}$. The temporal evolution of the magnetic field is described using the current vector potential $\mathbf{T}$, through the equation $\mathbf{J} = \nabla \times \mathbf{T}$. The electric field is functionally determined as $\mathbf{E} = \mathbf{E}[\mathbf{J}]$, subject to the boundary condition $(\nabla \times \mathbf{E}) \cdot \mathbf{n} + (\partial_t \mathbf{B}) \cdot \mathbf{n} = 0$. To represent the currents in the STAR-rotor bars, the following restriction was applied: $\int J_{\text{bar},k} = 0 \; \forall k = 1, \ldots, 36$.

FEM was used to precisely determine the maximum permissible current within the stator winding as a function of the applied voltage. This threshold is set at 70 V due to increased levels of magnetic reluctance, as shown in the findings presented in Fig. 8. A slight discrepancy is observed between the results obtained from FEM and those from a numerical solution of the equations using nodal circuits. When a maximum voltage of 50 V at 50 Hz was applied to the primary winding of the model, with a corresponding slip of 0.02, the resulting rms current was 8 A, yielding a quasi-synchronous torque of 0.96 Nm. The configuration of the poles and the distribution of the magnetic flux density are illustrated in Fig. 9.

The magnetic flux density reached a maximum of 0.4 T within the air gap and 0.2 T at the surface of the rotor, according to Fig. 10. The normalized current density, represented as J_z/J_c, along a central tape of the HTS rotor bar, together with the electric field distribution, is shown in Fig. 11. The distribution of induced currents, as illustrated in Fig. 12, reflects uniform magnetization across the HTS bars, which means an effective

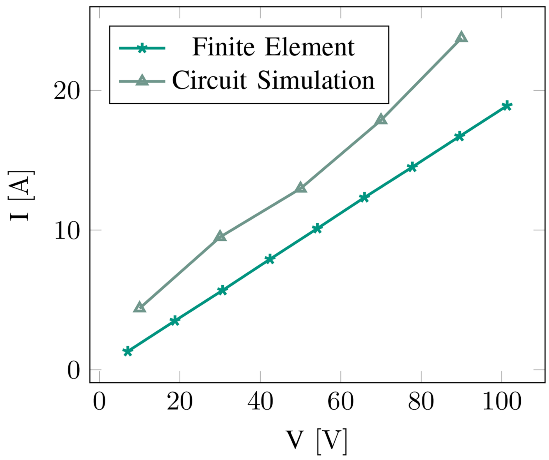

Fig. 8. Calculated current versus voltage curves of the motor at no-load ($Z_{\text{eq}} = 1.24\Omega + j3.65\Omega$).

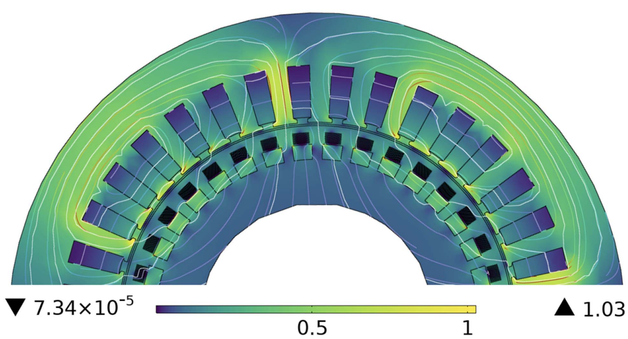

Fig. 9. Magnetic flux density [T] in half of the cross section of the STAR-machine.

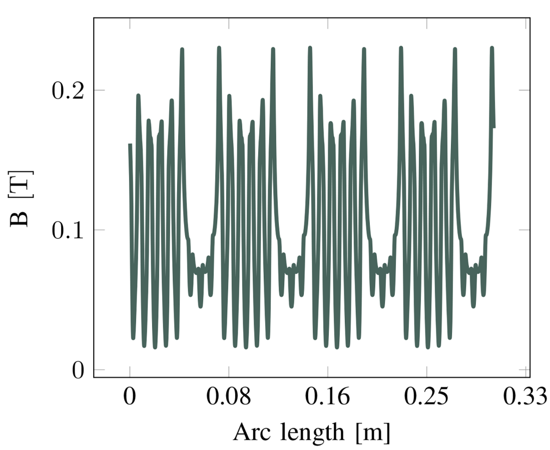

Fig. 10. Magnetic flux density at the rotor outer radius versus circumference.

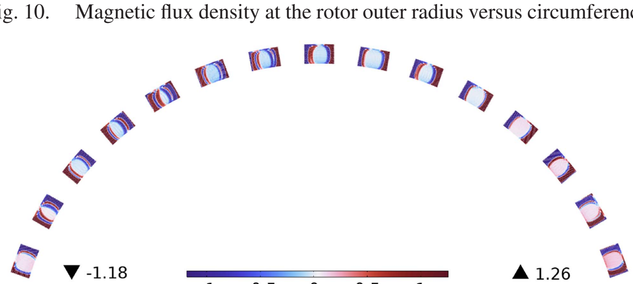

Fig. 11. Normalized current density in the bars (HTS-stacks) in half of the cross section.

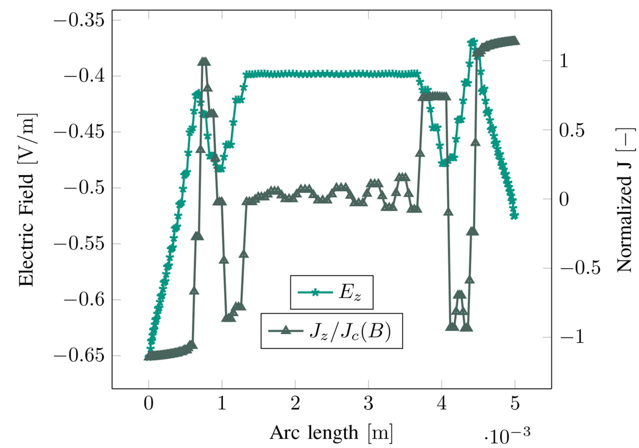

Fig. 12. Electric field and normalized current density in a bar of the rotor.

redistribution of current under the specified operating conditions.

D. Analytical Considerations

Following the arguments presented in [42], the inductive torque produced by a superconducting rotor pole is described by

$$T_{i,\text{pole}} = \frac{(\mathbf{A}_{\text{pole}} \cdot \mathbf{B}_{s,\text{pole}})^2}{2L_{\text{pole}}} \tag{17}$$

with the area of the pole A_{pole}, the magnetic field at the pole $B_{s,\text{pole}}$, and the inductance of the pole L_{pole}. The inductance L_{pole} is calculated following the expression for a rectangular current loop given by [43]. Area and magnetic field are considered as vectors to account for the angular variation during rotation. Integration over full angular scale and summation over all poles Q_r yields for the total torque and corresponding power

$$T_{i,\text{total}} = \frac{(\mathbf{A}_{\text{pole}} \cdot \mathbf{B}_{s,\text{pole}})^2}{L_{\text{pole}}} \cdot Q_r \tag{18}$$

$$P_{i,\text{total}} = T_{i,\text{total}} \cdot v_r. \tag{19}$$

For the realized STAR-rotor, these yields A=0.005 m·0.135 m = 0.675·10^{-3} m^2; L_{pole}=5.1184·10^{-8}H; $B_{s,\text{pole}}$=0.2 T; Q_r = 36 and finally

$$T_{i,\text{total}} = 13 \text{ Nm} \tag{20}$$

$$P_{i,\text{total}} = 121 \text{ W}. \tag{21}$$

These values are not too far off from the experimental results. The analytical formulas assume a homogeneous current distribution across all tapes, and do not consider the variation in current distribution as a function of the bar's position relative to the rotating magnetic field (cf., J/J_c of the HTS tapes in Fig. 11). It has to be noted that due to the high operating temperature $\geq$77 K (and especially in asynchronous operation), there is no torque contribution by frozen magnetization expected. In asynchronous operation, due to the relatively high electric fields, an HTS is operated in the steep regime of the E–I-curve (see Fig. 2). This

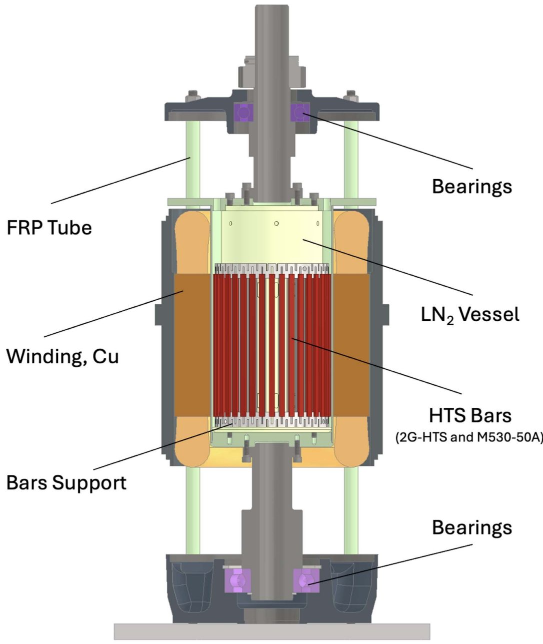

Fig. 13. Schematic cross section of the simple test stand.

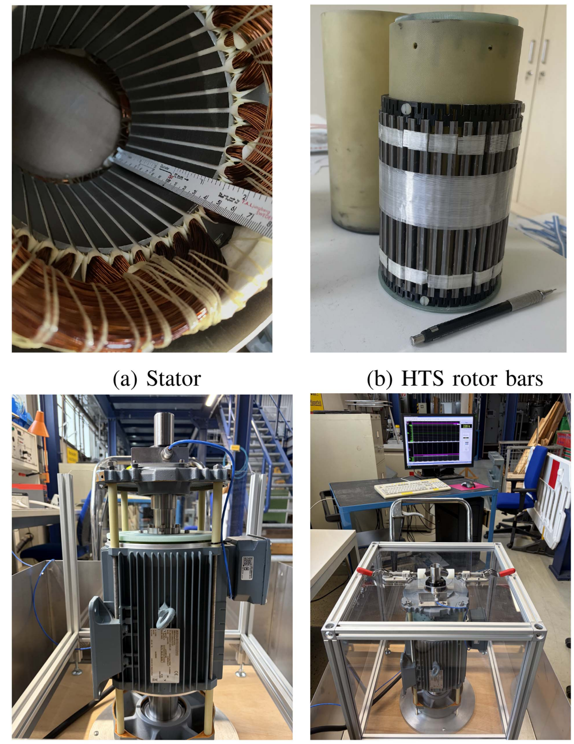

(a) Stator (b) HTS rotor bars

(c) STAR-motor (d) Workbench

Fig. 14. View into the stator (a), the inner rotor body with the bars attached (silver bandage to be removed after impregnation) (b), the assembled STAR-machine (c) and the completed test stand (d). (a) Stator. (b) HTS rotor bars. (c) STAR-motor. (d) Workbench.

AC environment does not allow a frozen magnetization requiring low electric fields and a quasi-DC situation.

III. Experimental Results

A simple experimental setup was designed for validating the motor concept, as depicted in Fig. 13. The motor shaft was vertically oriented to facilitate the basic cooling concept, which involves filling the LN_2 through the hollow central shaft. The cryogenic enclosure (FRP) houses the HTS rotor bars, and the inner wall provides holes to exchange LN_2 between the central reservoir and the section enclosing the bars.

The HTS rotor comprises 36 bars, each integrating 15 2G-HTS tapes (width $w = 5$ mm) layered over eight electrical steel laminations (M530-50 A). The rotor is supported by mechanical bearings situated at both shaft ends to separate from the cold section as much as possible. The design of the motor focuses on easy preparation and assembly while proving the concept, and is far from being optimized in electromagnetic respects.

Fig. 14 illustrates the constructed prototype of the STAR-machine. Detailed depictions of the conventional stator and the HTS rotor are provided, along with the fully integrated assembly. The testing apparatus was enclosed entirely to prevent uncontrolled exhaust of cryogenic media and to mount a mechanical brake.

The motor is operated using a variable frequency drive characterized by the following principal specifications: a rated output power of 8.7 kVA, efficiency losses of equal to 2.2% within the load range of 90%–100%, an output voltage span ranging from 0 to U_{IN}, and an output frequency range of 0–599 Hz. The device exhibits a nominal output current of 12.5 A, a maximum output current capacity of 18.75 A, and an overload capacity of 150%. A simplified scalar control strategy, specifically V/Hz, was employed throughout the experimental procedures. The onboard instrumentation provides the real-time measurement of pertinent electrical parameters.

A. Blocked Rotor Test

The rotor was immobilized using a mechanical brake that directly fixed the shaft. With the slip factor $s = 1$, a voltage was applied that corresponded to the supply frequency 50 Hz. Under these circumstances, the magnetization of the HTS rotor is achieved exclusively through the primary winding, thereby inducing maximal currents within the bars. As a result of the elevated secondary reluctance, which is comparable to that observed in no-load conditions because of the rotor's composition of residual ferromagnetic material, the stator current amplitude reaches significantly elevated magnitudes—Fig. 15 shows a peak stator current of 9 A and peak voltage of 40 V, accompanied by an inductive power factor of 0.43 and an active power of 134 W.

Fig. 16 shows the relationship between the stator current and the applied voltage over a range of low frequencies. The employment of scalar (V/Hz) control results in the terminal voltage exhibiting a linear relationship with frequency.

B. Dynamic Test

The initiation of the motor involved the application of voltage through a scalar control methodology, where the supply frequency was incrementally increased from zero to 50 Hz,

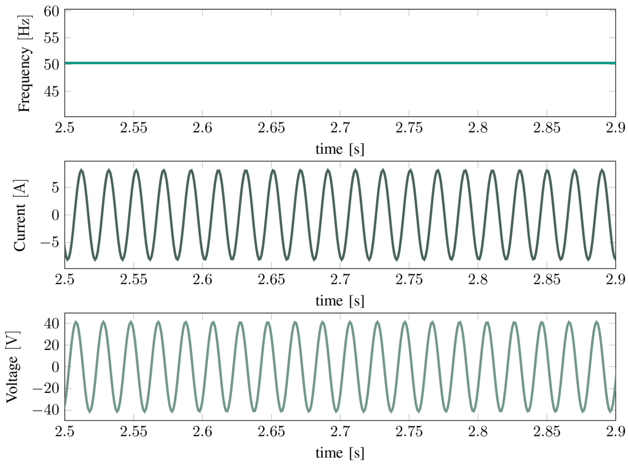

Fig. 15. Voltage and current results in the locked rotor test.

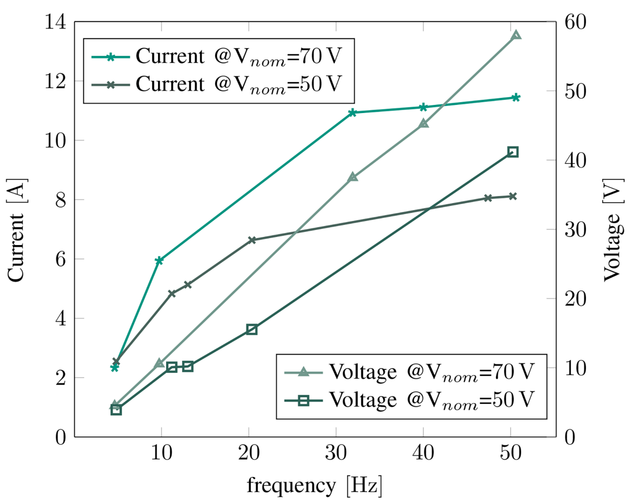

Fig. 16. Stator current versus frequency for slip $s = 1$.

enabling a controlled acceleration process. Subsequently, the motor was decelerated to a complete halt. A capacitive sensor, functioning as a resolver, was utilized to provide quadrature pulses for feedback on the rotor's angular position. From these data the instantaneous angular velocity v_r, expressed in revolutions per minute, was calculated according (22)

$$v_r = \frac{N_{\text{th}}}{k\Delta t} \tag{22}$$

where N_{th} is the number of pulses counted, k is the number of pulses per full rotation, and Δt is the time between pulses.

Fig. 17 shows the observed waveforms during the deceleration phase of the dynamic test, which was executed with an initial voltage supply of 50 V at a frequency of 50 Hz. The drive frequency decreases linearly from 50 Hz to approximately 30 Hz over a duration of 2.4 s, which confirms the controlled V/Hz scalar deceleration strategy. As the frequency decreases, both current and voltage amplitudes decrease gradually, while maintaining quasi-sinusoidal waveforms with minimal distortion. This observation indicates stable HTS rotor performance under varying slip conditions.

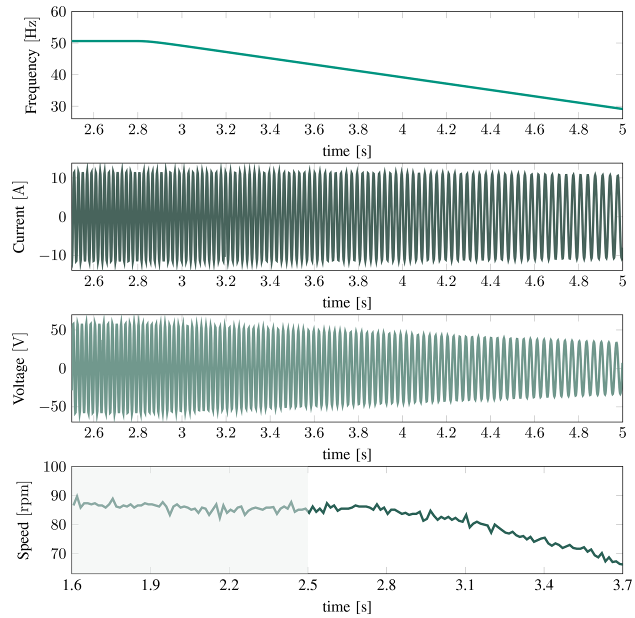

Fig. 17. Dynamic test results.

Under the nominal operating condition of 50 Hz, the rms value of the stator current was determined to be approximately 7.1 A. This resulted in an inductive power factor of 0.31 and an active power of approximately 128 W. The bottom diagram in Fig. 17 shows the rotor speed, which has been adjusted in time to align with the time base. The rotor speed exhibited a decrease from approximately 90 r/min at t =2.6 s to approximately 65 r/min, which corresponds closely to the anticipated reduction in synchronous speed.

The speed diagram (from t =2.5 s to t =3.7 s, Fig. 17) exhibits precise alignment with the voltage and current waveforms presented above, thereby confirming the temporal correspondence following postprocessing adjustments. The minor oscillations observed in the velocity curve ($\pm$3 r/min) are attributed to mechanical resonances and variations in the load torque (from bearings, windage, etc.); however, they do not significantly affect the overall dynamic response. These findings confirm the stable operation of the STAR-motor during transient deceleration, where induced currents in the superconducting bars efficiently maintain torque production at reduced speeds without excessive thermal heating, thereby preventing a superconducting-to-normal-conducting transition.

C. Experimental Trials At Room Temperature

When trying to activate the machine without LN_2 cooling, no rotation could be initiated.

IV. Discussion and Conclusion

This work, conducted through experiments and basic analysis, has demonstrated that it is possible to simplify conventional squirrel cage machines by utilizing appropriate 2G-HTS stacks without end-rings in a simple rotor architecture (STAR-machine).

TABLE II
COMPARISON OF MOTOR PERFORMANCE RESULTS ACROSS DIFFERENT METHODS

Parameter	Exp.	Analytical	Simulation	Eq. Circuit
Input Power [W]	128 / 134	–	150	$\sim$155
Output Power [W]	–	121	147	147
Slip s [-]	0.94 / 1.0	0.94	0.02	$\sim$0 / 0.049
Speed [r/min]	90 / 0	90	1470	$\sim$1500 / 1426
Torque [N m]	–	13	0.96	0.94 / 7.91

Preliminary tests have successfully demonstrated that this novel motor type can achieve stable operation. This motor presents a viable alternative to traditional rare-Earth magnet or wound-field synchronous machines, as it can achieve similar torque performance at synchronous speed without adding complexity through controlled excitation current. Experimental trials conducted at ambient temperature indicate that the ohmic components of only tiny thickness [see (3)] as well as the ferromagnetic lamination positioned behind the stacks [44] will not contribute considerably to the initiation torque. A more sophisticated experiment at controlled temperature just above T_c (e.g., 95 K) might prove that, but is not feasible with the present test stand. Table II summarizes the motor performance results obtained through experimental measurements, analytical modeling, finite element simulation, and equivalent circuit analysis.

The simple construction and the limited sealing of the test stand triggered considerable issues in thermal stresses in the bearings and humidity freezing. Bearing shrinkage and ice formation in the affected region introduce parasitic losses that compromise overall machine performance. These phenomena were partially mitigated by the installation of a localized heat source intended to suppress ice accretion; however, this measure was likely insufficient to fully counteract the thermally induced mechanical contraction (shrinkage) of the bearings. Although no direct evidence of air gap ice accumulation was detected, and the joule heating within the stator likely inhibits the formation of obstructive layers in the air gap, the potential for subtle frictional contributions from localized frost cannot be entirely excluded.

However, the simple construction and the small amount of heavy structural and magnetic material offer the potential to achieve high specific power for future machines. Considering the same rated output power of 4 KW, for instance, the specific power reaches 0.11 KW/Kg, which represents an increase of 20.4% compared to the original value of 0.091 kW/kg. This falls within the typical range of modern high-density motors, such as the SynRM IE5, the lightweight permanent magnet synchronous machine (PMSM), or compact traction motors. It should be noted that the commercial stator employed was not originally designed for high-performance applications, as it belongs to a standard low-power induction motor. Consequently, the results indicate that significantly higher gains remain achievable through the adoption of a stator specifically optimized for elevated performance.

LN_2 cooling of the rotor not only maintains the HTS tapes at 77 K but also significantly lowers the stator operating temperature by providing additional passive cooling that can increase the stator current density by up to a factor of 7.

Despite the prototype exhibiting the expected electromagnetic behavior as forecasted by design phase simulations, its overall performance currently cannot compete with commercially available machines, so far. This gap primarily arises from the reduced power rating of the laboratory-scale drive; the motor's electrical and magnetic circuitry necessitates a higher stator current than a conventional machine with the identical primary windings.

The chosen number of HTS bars and the configuration of the back-iron, although operating at the edge of functional design parameters, confirmed the fundamental concept. Nevertheless, the secondary ferromagnetic packet requires significant revision to decrease magnetic reluctance.

The test bench will undergo enhancements that incorporate closed-loop vector control, an inline torque transducer, and programmable load emulation to facilitate a comprehensive characterization of transient and steady-state performance. From a macroscopic modeling perspective, the operational principle, particularly with respect to startup dynamics, load transients, and the potential for four-quadrant operation of the HTS machine, will stimulate in-depth theoretical and experimental investigation. Future work will use the test stand to study the performance of other architectures of the STAR-machine, as well as different control strategies.

ACKNOWLEDGMENT

The authors would like to thank F. Gretschmann, R. Ernst, P. Heger, F. Emadi, and F. Hornung.

Author Contributions

Roberto Oliveira: conceptualization, formal analysis, investigation, methodology, validation, data curation, software, and writing the original draft. *Tabea Arndt:* conceptualization, formal analysis, methodology, supervision, funding acquisition, and writing–review and editing. *Andrés Yenes:* investigation, writing–review and editing. *Matthias Eisele:* conceptualization and resources. *Marion Kläser:* project administration and resources.

REFERENCES

[1] W. Nick et al., "380 kW synchronous machine with HTS rotor windings—-development at Siemens and first test results," *Physica C: Supercond.*, vol. 372–376, pp. 1506–1512, Aug. 2002.

[2] W. Nick, M. Frank, G. Klaus, J. Frauenhofer, and H.-W. Neumuller, "Operational experience with the world's first 3600 rpm 4 MVA generator at Siemens," *IEEE Trans. Appl. Supercond.*, vol. 17, no. 2, pp. 2030–2033, Jun. 2007. [Online]. Available: https://ieeexplore.ieee.org/document/4277627/

[3] W. Nick, J. Grundmann, and J. Frauenhofer, "Test results from Siemens low-speed, high-torque HTS machine and description of further steps towards commercialisation of HTS machines," *Physica C: Supercond. Appl.*, vol. 482, pp. 105–110, Nov. 2012. [Online]. Available: https://linkinghub.elsevier.com/retrieve/pii/S0921453412002079

[4] K. Kovalev et al., "Synchronous generator with HTS-2 G field coils for windmills with output power 1 MW," *J. Phys.: Conf. Ser.*, vol. 507, no. 3, May 2014, Art. no. 032023. [Online]. Available: https://iopscience.iop.org/article/10.1088/1742-6596/507/3/032023

[5] F. J. M. Dias, G. B. C. Carvalho, R. R. Schoenacher, G. d. Santos, F. Trillaud, and G. G. Sotelo, "Comparison of flux-trapped superconducting machine configurations," *IEEE Trans. Appl. Supercond.*, vol. 35, no. 5, Aug. 2025, Art. no. 5201605.

[6] L. F. D. Bucho, F. F. D. Silva, J. F. P. Fernandes, and P. J. C. Branco, "Electromechanical analysis of HTS cage rotors for induction-synchronous machines," *IEEE Trans. Appl. Supercond.*, vol. 34, no. 3, May 2024, Art.

no. 5201805, [Online]. Available: https://ieeexplore.ieee.org/document/10416365/

[7] T. Arndt et al., "Speedy_HTS–An HTS rotor for an uprated mid-speed wind power generator," *IEEE Trans. Appl. Supercond.*, vol. 36, no. 3, May 2026, Art. no. 5200104. [Online]. Available: https://ieeexplore.ieee.org/document/11197251/

[8] R. Köster, "Direct drive wind generators with superconducting excitation in the multi-MW class," Ph.D. dissertation, Dept. Elect. Eng. Inf. Technol., Inst. Electr. Energy Conversion, Electrical. Energy Conversion, Darmstadt, Germany, 2023.

[9] G. Morita, T. Nakamura, and I. Muta, "Theoretical analysis of a YBCO squirrel-cage type induction motor based on an equivalent circuit," *Supercond. Sci. Technol.*, vol. 19, no. 6, pp. 473–478, Jun. 2006. [Online]. Available: https://iopscience.iop.org/article/10.1088/0953-2048/19/6/011

[10] L. Wei, T. Nakamura, M. Yoshikawa, Y. Itoh, and T. Terazawa, "Comparison of different stator winding configurations of fully high-temperature superconducting induction/synchronous motor," *IEEE Trans. Appl. Supercond.*, vol. 30, no. 4, Jun. 2020, Art. no. 5205204. [Online]. Available: https://ieeexplore.ieee.org/document/9057628/

[11] T. Nakamura et al., "Load test and variable speed control of a 50-kW-Class fully superconducting induction/synchronous motor for transportation equipment," *IEEE Trans. Appl. Supercond.*, vol. 29, no. 5, Aug. 2019, Art. no. 5203005. [Online]. Available: https://ieeexplore.ieee.org/document/8656516/

[12] K. Ikeda et al., "Hysteretic rotating characteristics of an HTS induction/synchronous motor," *IEEE Trans. Appl. Supercond.*, vol. 27, no. 4, Jun. 2017, Art. no. 5203205. [Online]. Available: https://ieeexplore.ieee.org/document/7859290/

[13] J. Pinto, F. Gregorio, R. Oliveira, X. Granados, A. Alvarez, and J. Murta-Pina, "Preliminary analysis of core losses and performance of an axial flux motor with high temperature superconducting tapes on the rotor," in *Proc. Int. Young Engineers Forum*, Jul. 2022, pp. 25–32. [Online]. Available: https://ieeexplore.ieee.org/document/9850088/

[14] R. A. H. D Oliveira, O. Taalibi, and T. Arndt, "Compact HTS motor designs especially useful to be cooled by liquid hydrogen," *IEEE Trans. Appl. Supercond.*, vol. 34, no. 6, Sep. 2024, Art. no. 5203305. [Online]. Available: https://ieeexplore.ieee.org/document/10508049/

[15] R. Wang et al., "Preliminary design optimization of a fully superconducting motor based on disk-up-down-assembly magnets," *Supercond. Sci. Technol.*, vol. 36, no. 5, May 2023, Art. no. 054003. [Online]. Available: https://iopscience.iop.org/article/10.1088/1361-6668/acc822

[16] T. Tallerico, A. Anderson, and J. J. Scheidler, "Concept design of a 5 MW axial flux partially superconducting electric machine," in *Proc. AIAA AVIATION FORUM AND ASCEND 2024*, 2024, Art. no. 4092.

[17] C. C. Chow, M. D. Ainslie, and K. Chau, "High temperature superconducting rotating electrical machines: An overview," *Energy Rep.*, vol. 9, pp. 1124–1156, Dec. 2023. [Online]. Available: https://linkinghub.elsevier.com/retrieve/pii/S2352484722025628

[18] B. M. O. Santos, F. J. M. Dias, F. Trillaud, G. G. Sotelo, and R. D. Andrade Junior, "A review of technology readiness levels for superconducting electric machinery," *Energies*, vol. 16, no. 16, Aug. 2023, Art. no. 5955. [Online]. Available: https://www.mdpi.com/1996-1073/16/16/5955

[19] T. Balachandran et al., "Advancements in superconducting electric propulsion: Comparative analysis and progress update of CHEETA and CRUISE motors," *IEEE Trans. Appl. Supercond.*, vol. 35, no. 5, Aug. 2025, Art. no. 5203105.

[20] W. Chen, Y. Yan, Y. Qi, M. Huang, and W. Li, "Recent development of aircraft electric propulsion system: A technical review," *CES Trans. Elect. Mach. Syst.*, vol. 9, no. 1, pp. 115–130, Mar. 2025.

[21] F. Weng, M. Zhang, T. Lan, Y. Wang, and W. Yuan, "Fully superconducting machine for electric aircraft propulsion: Study of AC loss for HTS stator," *Superconductor Sci. Technol.*, vol. 33, no. 10, 2020, Art. no. 104002.

[22] M. R. Koblischka, K. Berger, and H. Caron, "Superconductivity for railway applications: A review," *Energy Convers. Manage.: X*, vol. 28, 2025, Art. no. 101344.

[23] M. D. Ainslie, "Numerical modelling of high-temperature superconducting dynamos: A review," *Superconductivity*, vol. 5, 2023, Art. no. 100033. [Online]. Available: https://www.sciencedirect.com/science/article/pii/S2772830722000321

[24] M. Dam and T. Arndt, "Robotic winding of non-planar high-temperature superconducting coils," *Superconductor Sci. Technol.*, vol. 38, no. 12, 2025, Art. no. 125004.

[25] J. Pyrhonen, T. Jokinen, and V. Hrabovcová, *Design of Rotating Electrical Machines, 2nd ed.* Chichester, U.K.: Wiley, 2014.

[26] E. Berrospe-Juarez, F. Trillaud, V. M. R. Zermeno, and F. Grilli, "Electromagnetic modeling of large-scale high-temperature superconductor systems," 2020. [Online]. Available: https://arxiv.org/abs/2006.02033

[27] J. Bardeen and M. Stephen, "Theory of the motion of vortices in superconductors," *Phys. Rev.*, vol. 140, no. 4A, 1965, Art. no. A1197.

[28] B. Dutoit, F. Grilli, and F. Sirois, "Numerical Modeling of Superconducting Applications: Simulation of Electromagnetics, Thermal Stability, Thermo-Hydraulics and Mechanical Effects in Large-Scale Superconducting Devices, 1st ed., ser. World Scientific Series in Applications of Superconductivity and Related Phenomena," Singapore: World Sc., 2023. [Online]. Available: https://www.worldscientific.com/worldscibooks/10.1142/13282

[29] F. Grilli, "Numerical modeling of HTS applications," *IEEE Trans. Appl. Supercond.*, vol. 26, no. 3, Apr. 2016, Art. no. 0500408. [Online]. Available: https://ieeexplore.ieee.org/document/7387708/

[30] J. Geng et al., "Origin of DC voltage in type II superconducting flux pumps: Field, field rate of change, and current density dependence of resistivity," *J. Phys. D: Appl. Phys.*, vol. 49, no. 11, Mar. 2016, Art. no. 11LT01. [Online]. Available: https://iopscience.iop.org/article/10.1088/0022-3727/49/11/11LT01

[31] W. T. Norris, "Calculation of hysteresis losses in hard superconductors carrying AC: Isolated conductors and edges of thin sheets," *J. Phys. D: Appl. Phys.*, vol. 3, no. 4, pp. 489–507, Apr. 1970. [Online]. Available: https://iopscience.iop.org/article/10.1088/0022-3727/3/4/308

[32] M. Oomen, "AC Loss in Superconducting Tapes and Cables," Ph.D. thesis, Univ. Twente, Enschede, The Netherlands, 2000.

[33] Z. Jiang, K. Hamilton, N. Amemiya, R. A. Badcock, and C. W. Bumby, "Dynamic resistance of a high-TC superconducting flux pump," *Appl. Phys. Lett.*, vol. 105, no. 11, Sep. 2014, Art. no. 112601. [Online]. Available: https://pubs.aip.org/apl/article/105/11/112601/132769/Dynamic-resistance-of-a-high-Tc-superconducting

[34] J. R. Clem, "Inductances and attenuation constant for a thin-film superconducting coplanar waveguide resonator," *J. Appl. Phys.*, vol. 113, no. 1, 2013, Art. no. 013910.

[35] S. Peng et al., "A fast inductance calculation method for equivalent circuit models of non-insulation superconducting coils," *Eur. Phys. J. Special Top.*, vol. 234, no. 7, pp. 9931–9939, Mar. 2026.

[36] R. Meservey and P. M. Tedrow, "Measurements of the kinetic inductance of superconducting linear structures," *J. Appl. Phys.*, vol. 40, no. 5, pp. 2028–2034, 1969.

[37] B. Liu, S. Wang, B. Zhao, J. Fang, and X. Wang, "Analysis and calculation of LR circuit mathematical model for high temperature superconducting induction motor," *Physica C: Supercond. Appl.*, vol. 568, Jan. 2020, Art. no. 1353579. [Online]. Available: https://linkinghub.elsevier.com/retrieve/pii/S0921453419302606

[38] L. Mine, S. Goyal, and A. A. Abdallh, "Improved dynamic modeling of squirrel-cage induction machines using magnetic reluctance network theory," in *Proc. 21st Int. Conf. Elect. Mach. Syst.*, Oct. 2018, pp. 555–559. [Online]. Available: https://ieeexplore.ieee.org/document/8549370/

[39] T. Nakamura, H. Miyake, Y. Ogama, G. Morita, I. Muta, and T. Hoshino, "Fabrication and characteristics of HTS induction motor by the use of Bi-2223/Ag squirrel-cage rotor," *IEEE Trans. Appl. Supercond.*, vol. 16, no. 2, pp. 1469–1472, Jun. 2006.

[40] M. Ainslie et al., "A new benchmark problem for electromagnetic modelling of superconductors: The high-t_c superconducting dynamo," *Superconductor Sci. Technol.*, vol. 33, no. 10, Oct. 2020, Art. no. 105009. [Online]. Available: https://iopscience.iop.org/article/10.1088/1361-6668/abae04

[41] G. Santos, B. M. O. Santos, F. Trillaud, G. Hajiri, and K. Berger, "T–a–ϕ and j–a–ϕ formulations for efficient electromagnetic simulations of high-temperature superconductors in 2D," *Superconductor Sci. Technol.*, vol. 38, no. 4, 2025, Art. no. 045017.

[42] J. D. Jones and P. W. Matthews, "Three-phase superconducting motor," *Rev. Sci. Instrum.*, vol. 35, no. 5, pp. 630–633, May 1964. [Online]. Available: https://pubs.aip.org/rsi/article/35/5/630/460767/Three-Phase-Superconducting-Motor

[43] R. Dengler, "Self inductance of a wire loop as a curve integral," *Adv. Electromagn.*, vol. 5, no. 1, pp. 1–8, 2016.

[44] M. Biasion, I. S. P. Peixoto, J. F. P. Fernandes, S. Vaschetto, G. Bramerdorfer, and A. Cavagnino, "Iron loss characterization in laminated cores at room and liquid nitrogen temperature," in *Proc. Energy Convers. Congr. Expo.*, 2022, pp. 1–8.